Supplementary Information

Electrochemically in situ formed rocksalt phase in titanium dioxide determines pseudocapacitive sodium-ion storage

Dafu Tang[1,2,7], Ruohan Yu[3,7], Yalong Jiang[4,7], Jiantao Li[5,*], Zerui Yan[1,2], Sicheng Fan[1,2], Xiaojuan Huang[1,2], Sungsik Lee[6], Tianyi Li[6], Qingshui Xie[1,2], Liqiang Mai[3,*], Dong-Liang Peng[1,2,*], Qiulong Wei[1,2,*]

[1] Department of Materials Science and Engineering, Fujian Key Laboratory of Surface and Interface Engineering for High Performance Materials, College of Materials, Xiamen University, Xiamen 361005, P. R. China.

[2] Innovation Laboratory for Sciences and Technologies of Energy Materials of Fujian Province (IKKEM), Xiamen 361005, PR China.

[3] State Key Laboratory of Advanced Technology for Materials Synthesis and Processing, Wuhan University of Technology, Wuhan 430070, P. R. China.

[4] State Key Laboratory of New Textile Materials and Advanced Processing, Wuhan Textile University, Wuhan 430200, P. R. China.

[5] Chemical Sciences and Engineering Division, Argonne National Laboratory, Lemont, IL 60439, USA.

[6] X-ray Science Division, Argonne National Laboratory, Lemont, IL 60439, USA.

[7] These authors contributed equally: Dafu Tang, Ruohan Yu and Yalong Jiang.

[*]E-mail: jiantao.li@anl.gov; mlq518@whut.edu.cn; dlpeng@xmu.edu.cn; qlwei@xmu.edu.cn

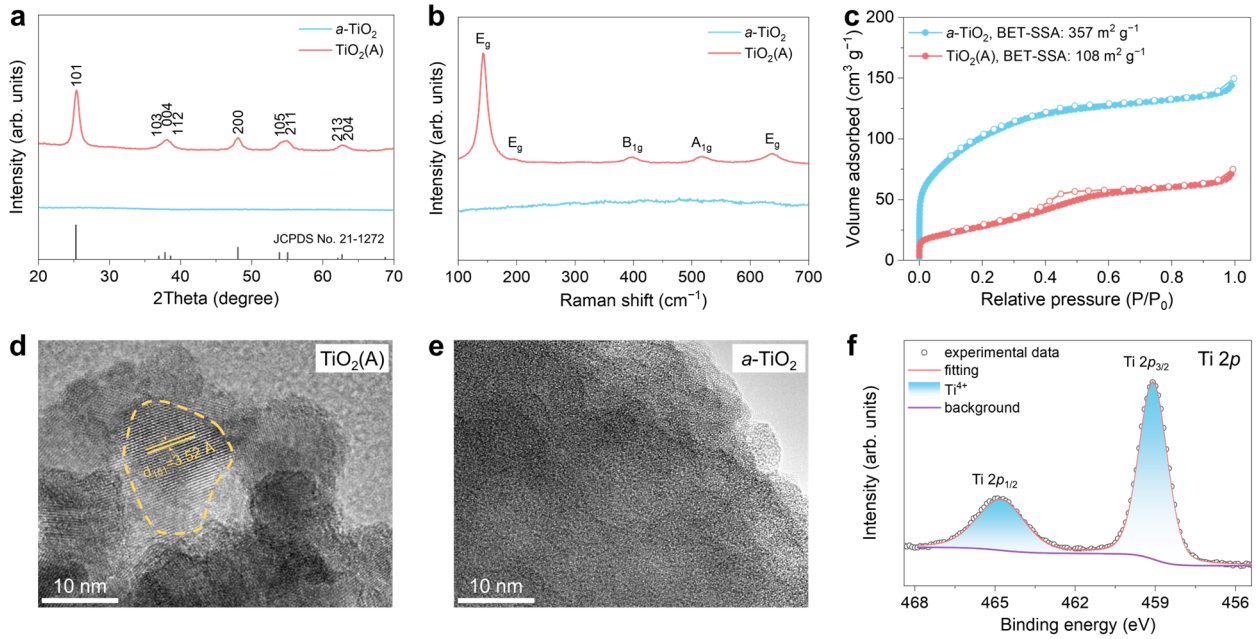

Supplementary Fig. 1. Characterization of TiO_2 samples. (**a**) XRD patterns, (**b**) Raman spectra and (**c**) nitrogen adsorption-desorption isotherms of the TiO_2(A) and *a*-TiO_2 samples. HRTEM images of (**d**) TiO_2(A) and (**e**) *a*-TiO_2. (**f**) The Ti 2*p* XPS spectrum of the *a*-TiO_2. The nanosized TiO_2(A) has an average grain size of ~10 nm (Supplementary Fig. 1a), according to the Scherrer Formula. The Raman spectra show the characteristic vibration peaks for TiO_2(A), and there are no peaks for *a*-TiO_2 (Supplementary Fig. 1b). The Brunauer-Emmett-Teller specific surface area (BET-SSA) of *a*-TiO_2 and TiO_2(A) samples is 357 and 108 m^2 g^{-1}, respectively (Supplementary Fig. 1c). HRTEM images (Supplementary Fig. 1d and 1e) show the crystalline TiO_2(A) nanograins and amorphous *a*-TiO_2.

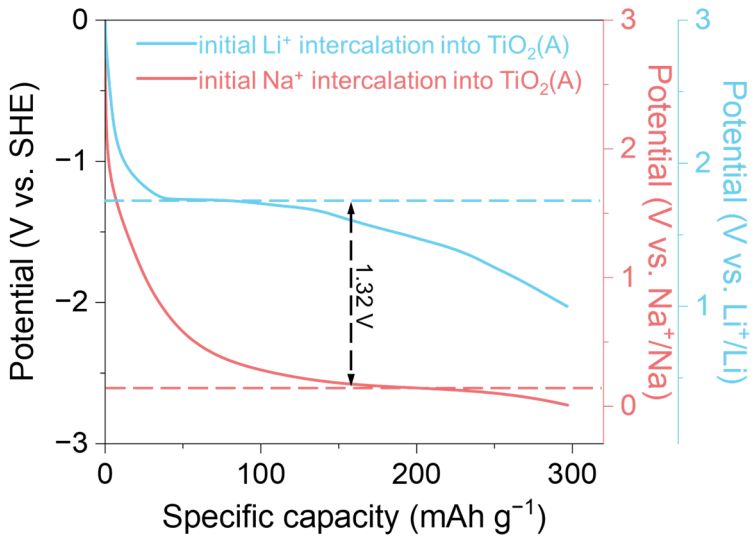

Supplementary Fig. 2. Initial intercalation of Na^+ and Li^+ into TiO_2(A). Li^+ can reversibly intercalate into TiO_2(A), displaying a flat plateau at ~1.75 V *vs*. Li^+/Li, that is −1.29 V *vs*. SHE. In contrast, the initial infusing of Na^+ in anatase lattices requires an additional electrochemical driving force to overcome a large potential gap of 1.32 V, accompanied by a crystalline to amorphous transition.

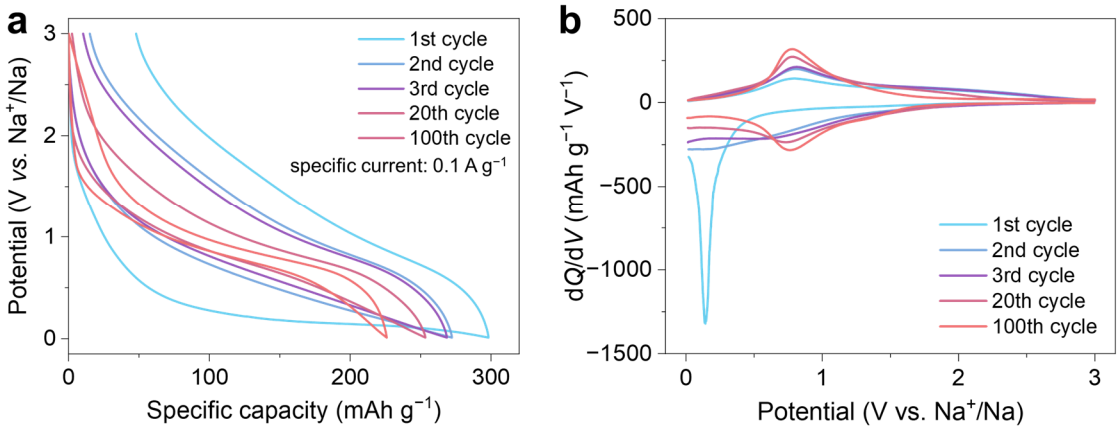

Supplementary Fig. 3. GCD profiles of the TiO_2(A) electrode. (**a**) GCD profiles and (**b**) corresponding dQ/dV plots of the TiO_2(A) electrode for the initial 100 cycles at 0.1 A g^{-1} in 0.01–3 V *vs*. Na^+/Na.

The continuously varying GCD profiles (Supplementary Fig. 3a) and differential capacity (dQ/dV) plots (Supplementary Fig. 3b) during the initial 20 cycles indicate a multistep phase transformation. After 20 cycles, the TiO_2(A) electrode delivers a reversible capacity of 253 mAh g^{-1}, corresponding to ~0.75 Na^+ per Ti. Then, the dQ/dV plots display a "mirror-like" shape and maintains stably for 20–100 cycles. The decreases of the voltage hysteresis indicate an electrochemical activation process.

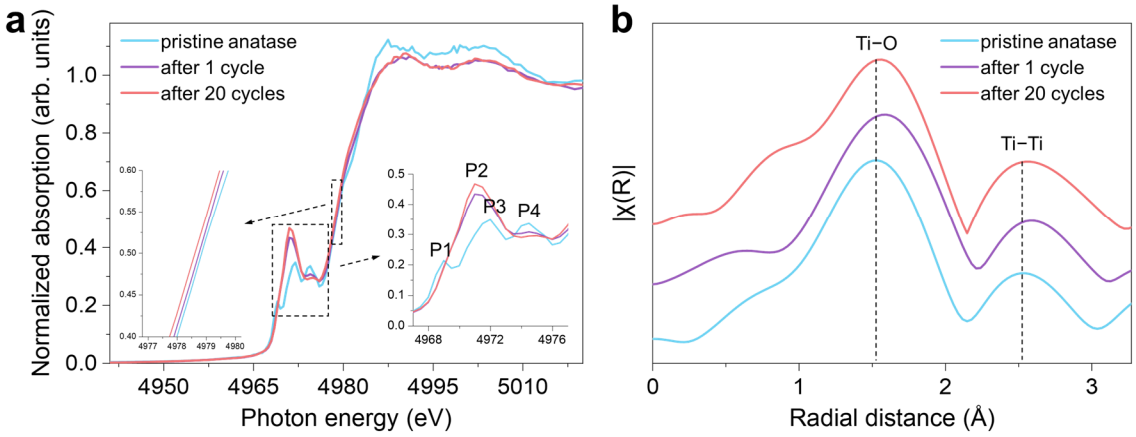

Supplementary Fig. 4. Ex situ XAS spectra of the TiO_2(A) electrode. (**a**) XANES of the TiO_2(A) electrode. The left inset is the enlarged absorption edge, and the right inset is the enlarged pre-edge peak. (**b**) Fourier-transformed Ti K-edge EXAFS spectra of the TiO_2(A) electrode during 20 cycles.

During the electrochemical cycles, the absorption edge of the active material gradually shifts towards low energy (the left inset in Supplementary Fig. 4a), which is attributed to the reduction of Ti^{4+}. The active material before cycling shows three split characteristic peaks of anatase in the pre-edge region, P1 at 4969.0 eV, P3 at 4972.0 eV and P4 at 4974.5 eV. Pl and P3 originate from the hybridization of 3*d*–4*p*, and P4 originate from the hybridization of 4*p*–4*s*. After 1 and 20 cycles, the active material exhibits single consolidated peak P2 at 4971.0 eV and broad P4 peak at 4974.5 eV, indicating the change of ordering structure (the right inset in Supplementary Fig. 4a). The drastic changes in the length of Ti–O and Ti–Ti pairs in EXAFS spectra (Supplementary Fig. 4b) indicate the electrochemically driven distortion and expansion of the octahedral coordination structure for accommodating Na^+ ions

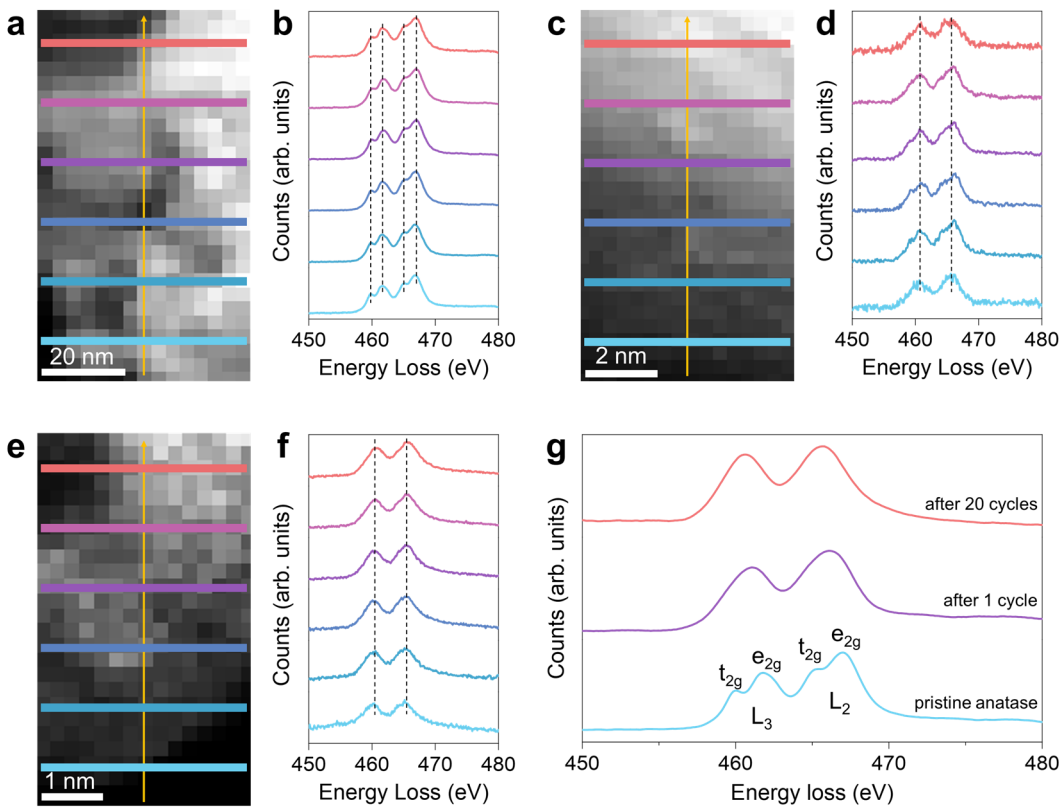

Supplementary Fig. 5. EELS spectra of TiO_2(A) after cycling. STEM images and corresponding EELS spectra of (**a**,**b**) pristine anatase, (**c**,**d**) after 1 cycle and (**e**,**f**) after 20 cycles. (**g**) The EELS spectra show that the structure changes from anatase to amorphous.

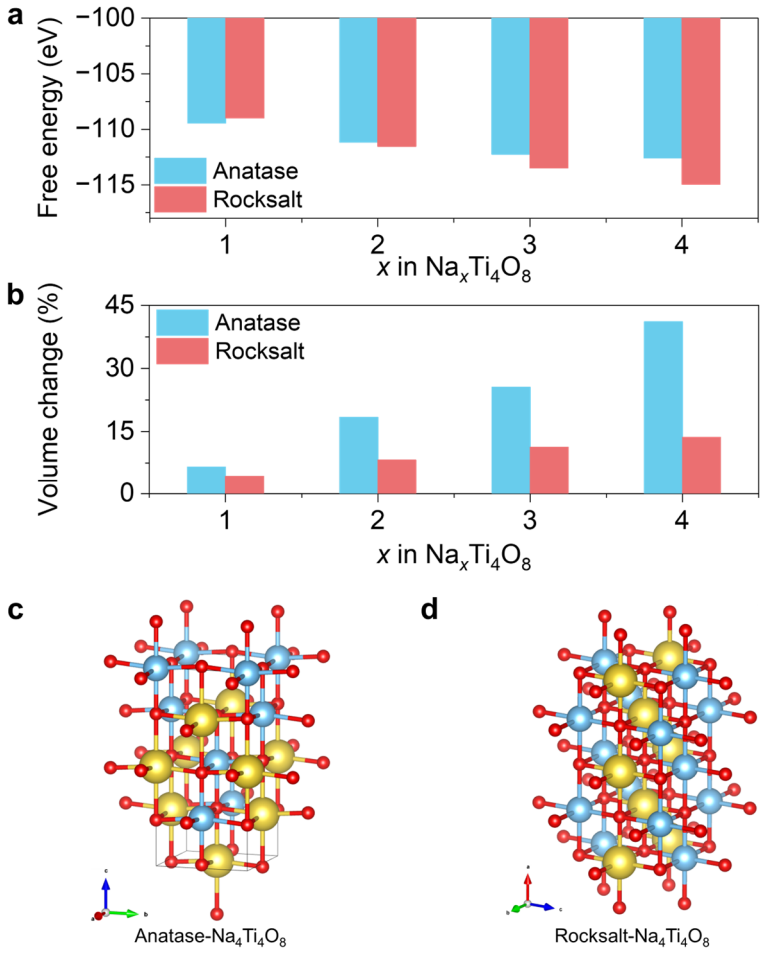

Supplementary Fig. 6. DFT calculation. The calculated (**a**) free energy and (**b**) volume change of anatase- and RS-$Na_xTi_4O_8$. The crystal structure of (**c**) anatase-$Na_4Ti_4O_8$ and (**d**) RS-$Na_4Ti_4O_8$.

The electrochemically-driven intercalation of Na^+ ions into anatase causes large volume expansion and lattices distortions, along with the decreased free energy. This could be regarded as the loss of orderings, that is the *c*-to-*a′* transformation process. Subsequently, the free energy of −114.943 eV for fully sodiated RS-$Na_4Ti_4O_8$ is lower than that of −112.569 eV for fully sodiated anatase-$Na_4Ti_4O_8$, indicating the energetically favorable of forming RS phase.

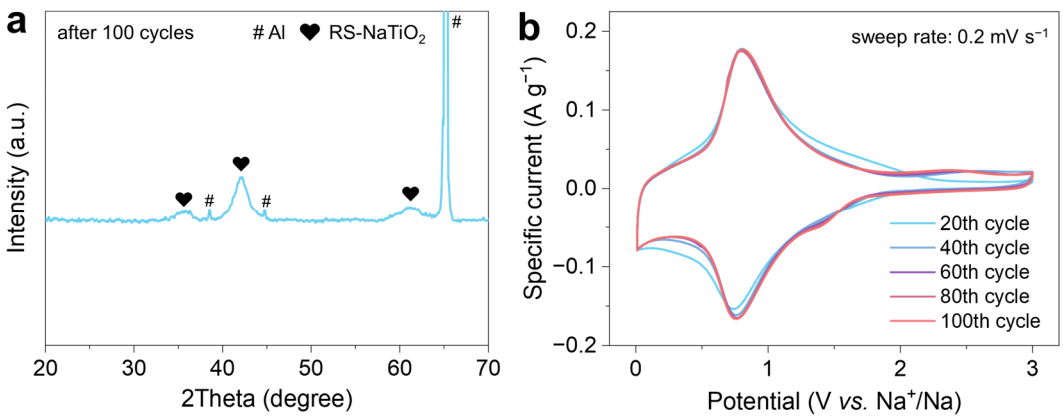

Supplementary Fig. 7. XRD pattern and CV curves of the TiO_2(A) electrode after 100 cycles. (**a**) XRD pattern of the TiO_2(A) electrode after 100 cycles. The XRD pattern indicate the cyclic stability of RS-$NaTiO_2$. (**b**) CV curves of TiO_2(A) electrode during 20 to 100 cycles at 0.2 mV s^{-1}.

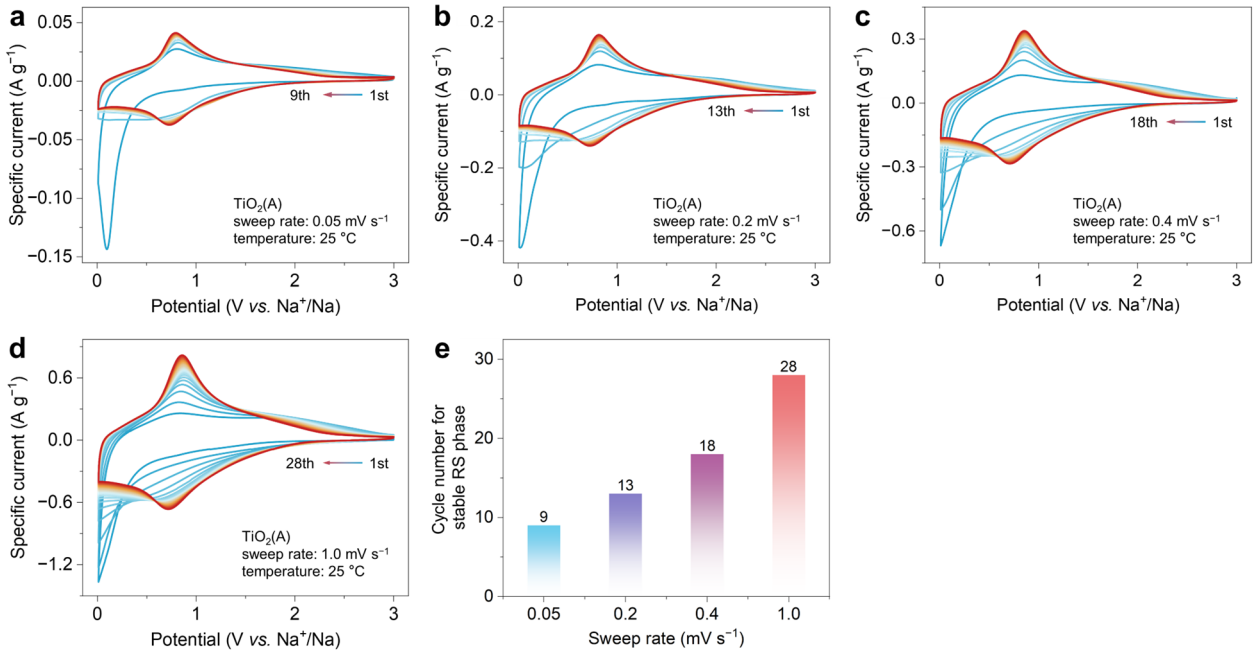

Supplementary Fig. 8. Effect of cycling rate on the *c-a'-RS* transformation kinetics. CV curves of the TiO_2(A) electrode at room temperature at the sweep rate of: (**a**) 0.05 mV s^{-1}, (**b**) 0.2 mV s^{-1}, (**c**) 0.4 mV s^{-1} and (**d**) 1.0 mV s^{-1}. (**e**) Cycle number of the TiO_2(A) electrode for the formation of stable RS phase.

The finish of *c-a'-RS* transformation is identified by checking the overlapping of CV shape after different cycles. The "mirror-like" CV shape of cycled TiO_2(A) electrode gets well overlapping after 6, 13, 20 and 28 cycles at the sweep rates of 0.05, 0.2, 0.4 and 1.0 mV s^{-1}, respectively. The transformation rate becomes slower with the increase of sweep rates, which is might owing to the insufficient sodiation (the decreased intercalation numbers of Na^+ ions into the lattices) at high sweep rates.

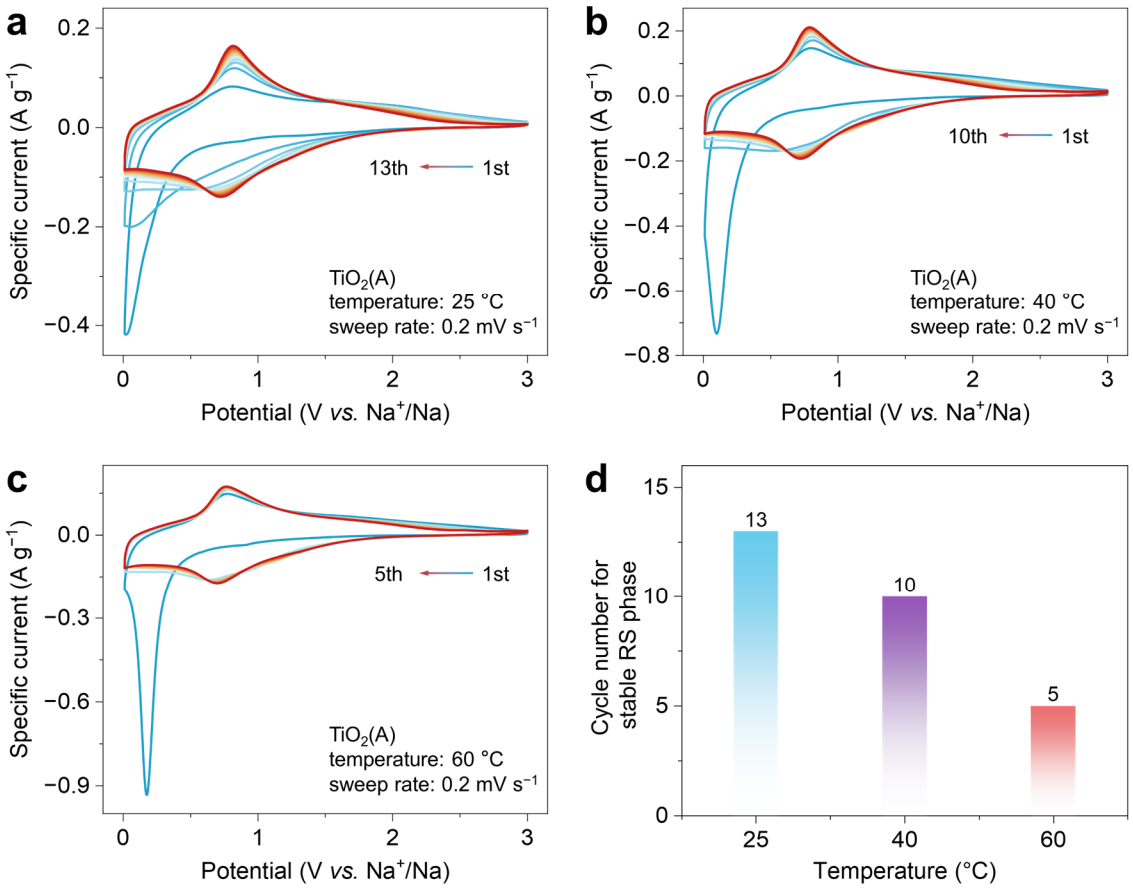

Supplementary Fig. 9. Effect of temperature on the *c-a'-RS* transformation kinetics. CV curves of the TiO_2(A) electrode at the sweep rate of 0.2 mV s^{-1} at temperature of (**a**) 25 °C, (**b**) 40 °C and (**c**) 60 °C. (**d**) Cycle number of the TiO_2(A) electrode for the formation of stable RS phase.

The "mirror-like" CV curves of the cycled TiO_2(A) electrode overlaps after 13, 10 and 5 cycles at the sweep rate of 0.2 mV s^{-1} at the temperature of 25, 40 and 60 °C, respectively. When the temperature is raised from 25 °C to 60 °C, the *c-a'-RS* transformation is accelerated, owing to the enhanced kinetics by increased temperature that promotes the re-arrangement of the atoms during *c-a'-RS* transformation.

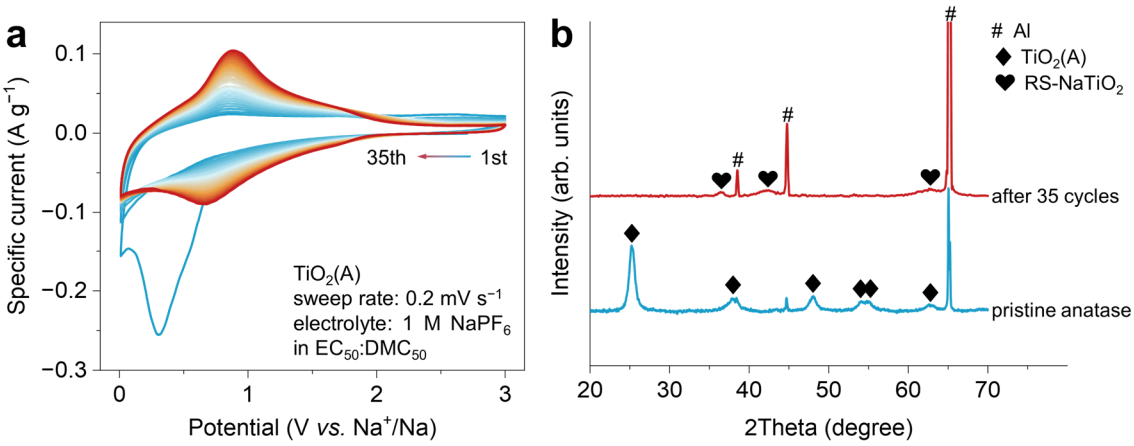

Supplementary Fig. 10. Electrochemical behavior of the TiO_2(A) electrode in carbonate electrolyte. (a) CV curves of the TiO_2(A) electrode measured in the electrolyte of 1 M $NaPF_6$ in EC_{50}:DMC_{50} at the sweep rate of 0.2 mV s^{-1}. (b) XRD patterns of the corresponding TiO_2(A) electrode before and after cycling.

In the carbonate electrolyte, the reduction peak at ~0.3 V in the 1st sodiation process corresponds to the irreversible amorphization reaction and the formation of SEI layers. The emerging redox couple near 0.8 V vs. Na^+/Na after 35 cycles. The ex-situ XRD pattern of the TiO_2(A) electrode after 35 cycles show the presence of RS phase. The CV curves in ester-based electrolyte show the similar shape and redox reaction potential compared to those results in ether-based electrolyte, indicating that the electrolyte system does not affect the *c*-*a*'-RS transformation. However, the serious decomposition of carbonate electrolyte and the formation of thick SEI layers lead to increased polarization.

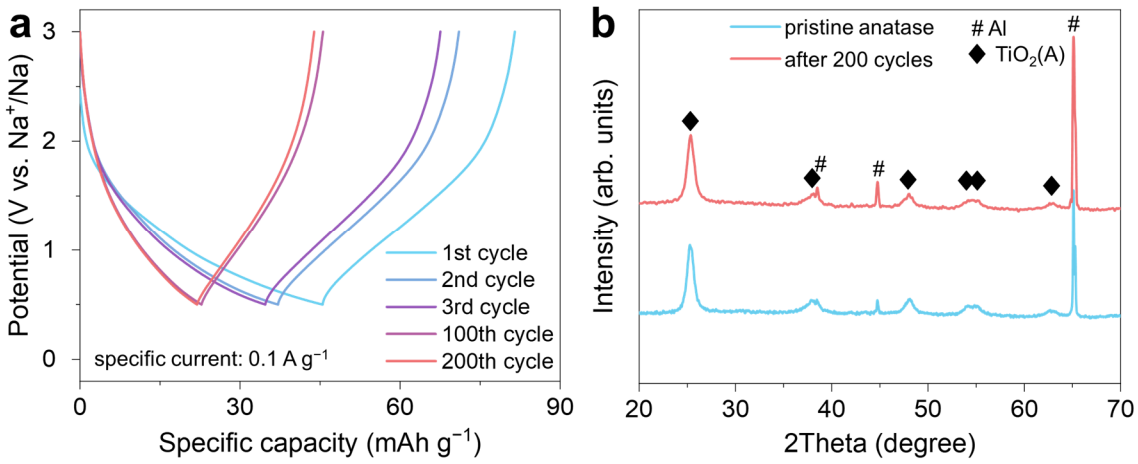

Supplementary Fig. 11. GCD profiles and XRD patterns of the TiO_2(A) electrode cycled in 0.5–3 V *vs.* Na^+/Na. (**a**) GCD profiles and (**b**) corresponding ex situ XRD patterns of the TiO_2(A) electrode directly cycled in 0.5–3 V *vs.* Na^+/Na at 0.1 A g^{-1} for the initial 200 cycles.

When the TiO_2(A) electrode was directly cycled in 0.5–3 V *vs.* Na^+/Na, the electrochemical anatase to amorphous transition was avoided, and the crystalline TiO_2(A) did not turn into RS phase even after 200 cycles, indicating the necessity of forming amorphous structures for further turning into RS phase.

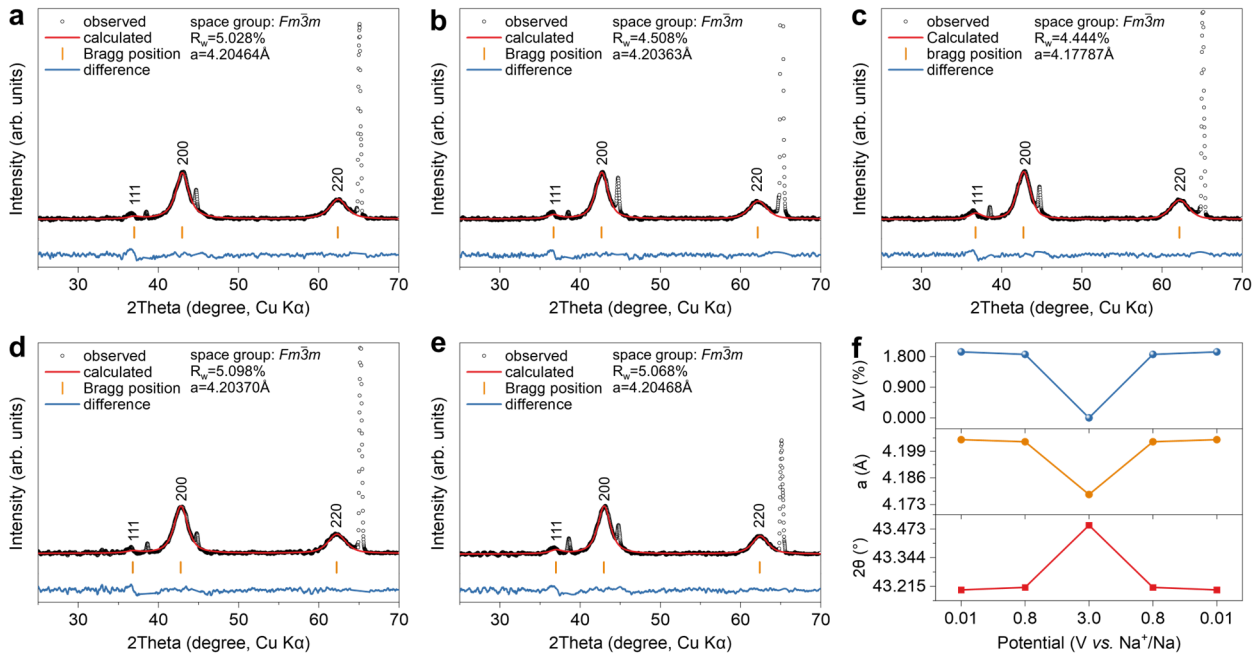

Supplementary Fig. 12. Rietveld XRD refinement. Rietveld-refined XRD patterns of the RS-$NaTiO_2$ (excluded diffraction peaks of the current collector) at different potentials: (**a**) sodiated at 0.01 V, (**b**) desodiated at 0.8 V, (**c**) desodiated at 3.0 V, (**d**) sodiated at 0.8 V and (**e**) sodiated at 0.01V, respectively. (**f**) Principal diffraction peak angle (2θ), lattice parameter (*a*), and volume changes (ΔV) of RS-$NaTiO_2$ during (de)sodiation based on the ex situ XRD results.

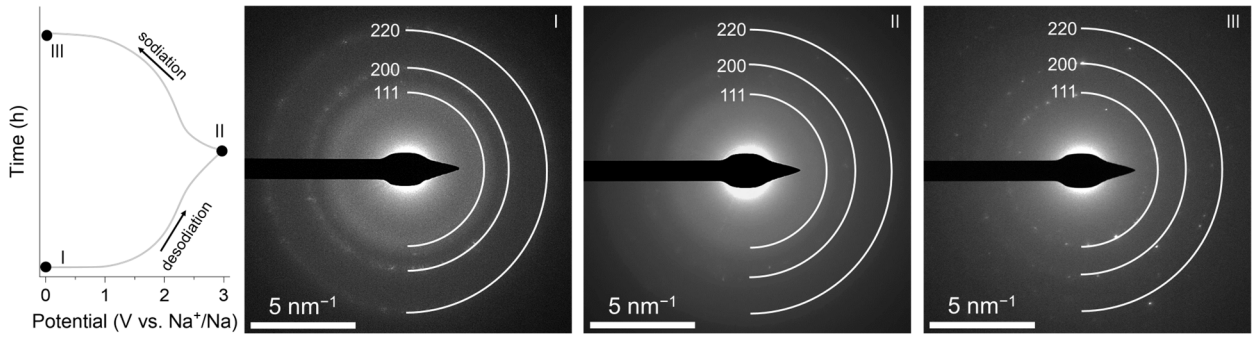

Supplementary Fig. 13. Ex situ SAED patterns of electrochemically formed *c-a'-RS*-$NaTiO_2$ (the TiO_2(A) electrodes after 20 cycles) at different sodiated and desodiated states.

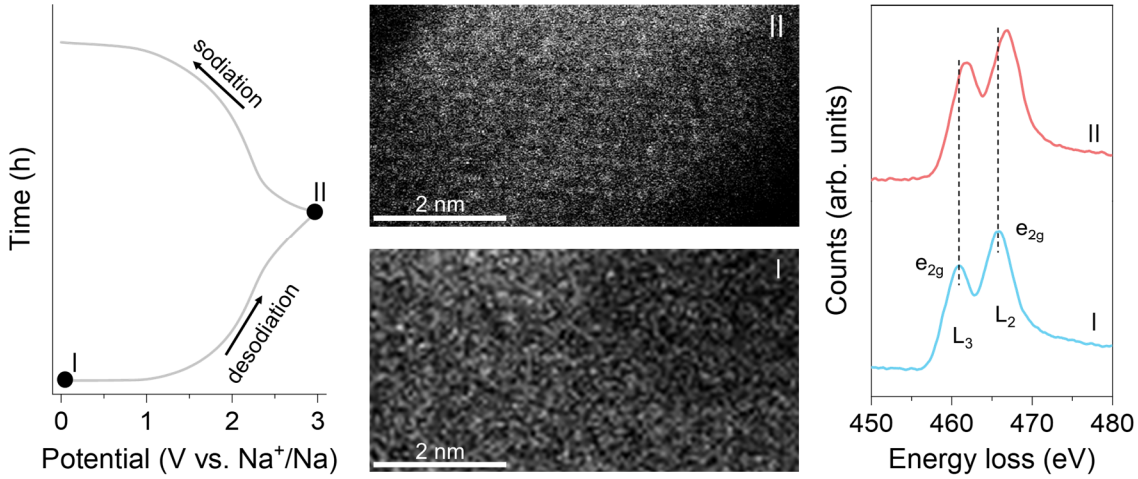

Supplementary Fig. 14. Ex situ EELS spectra of the *c-a'-RS*-$NaTiO_2$ (the TiO_2(A) electrode after 20 cycles) during sodiation and desodiation. The reversible peak shifts indicate the reversible redox couple of during (de)sodiation.

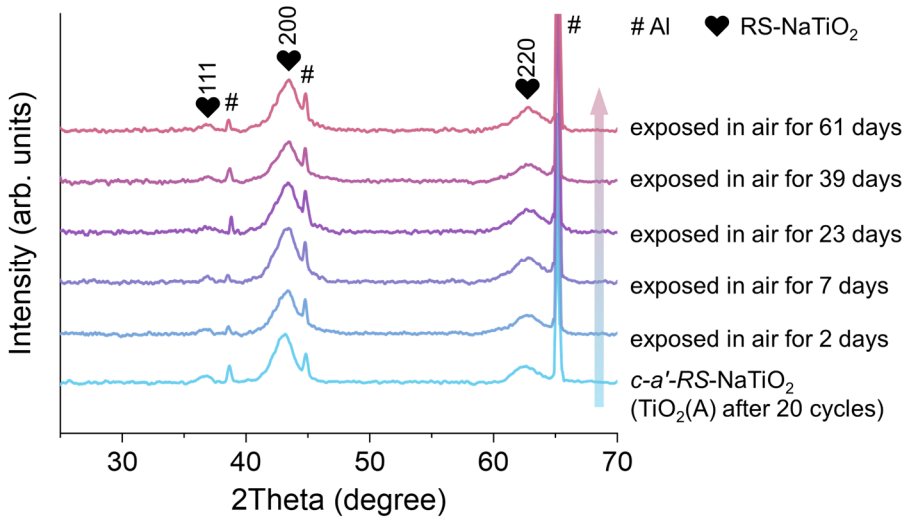

Supplementary Fig. 15. XRD patterns of the electrochemically formed *c-a'-RS*-$NaTiO_2$ (TiO_2(A) electrode after 20 cycles) under exposure to air for two months. The well-maintained XRD patterns indicate the air stability of RS-$NaTiO_2$.

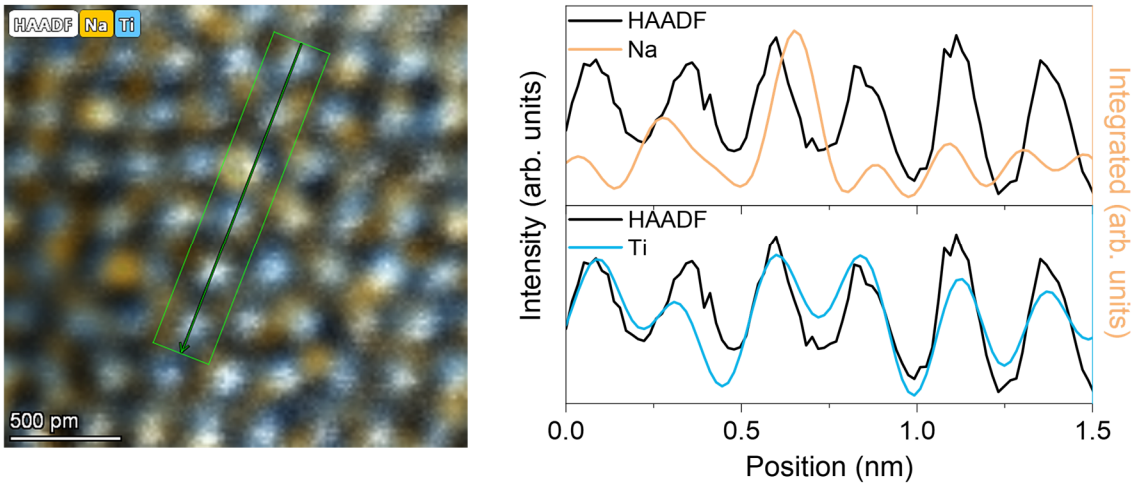

Supplementary Fig. 16. Linear scan elemental mapping of the RS-$NaTiO_2$ nanograins from different directions, indicating cation-disordering of the Na and Ti atoms at the octahedral (4a) sites.

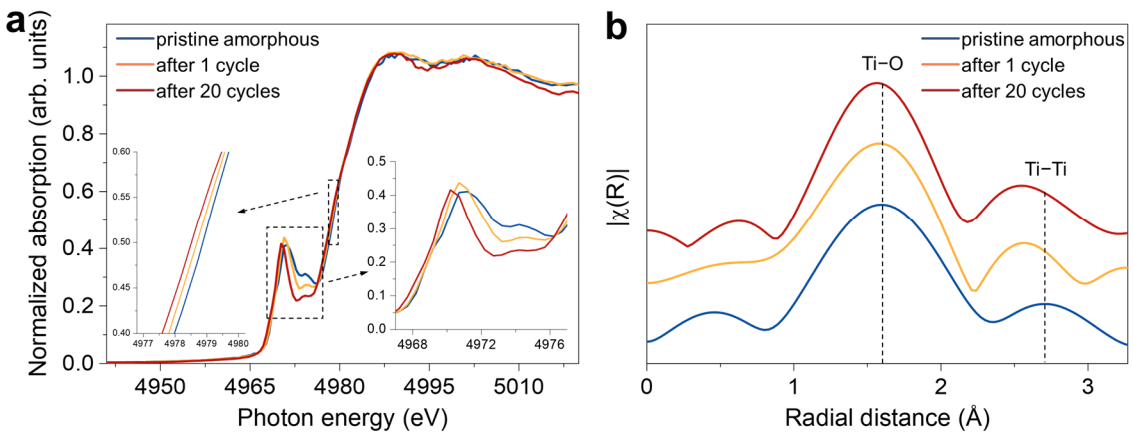

Supplementary Fig. 17. Ex situ XAS spectra of the *a*-TiO_2 electrode. (**a**) XANES of the *a*-TiO_2 electrode. The left inset is the enlarged absorption edge, and the right inset is the enlarged pre-edge peak. (**b**) Fourier-transformed Ti K-edge EXAFS spectra of the *a*-TiO_2 electrode during 20 cycles.

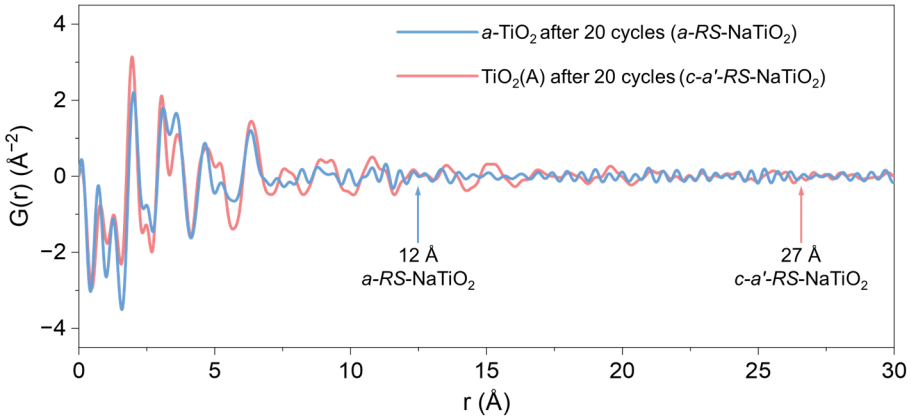

Supplementary Fig. 18. SRPDF spectra of the TiO_2(A) and *a*-TiO_2 electrodes after 20 cycles.

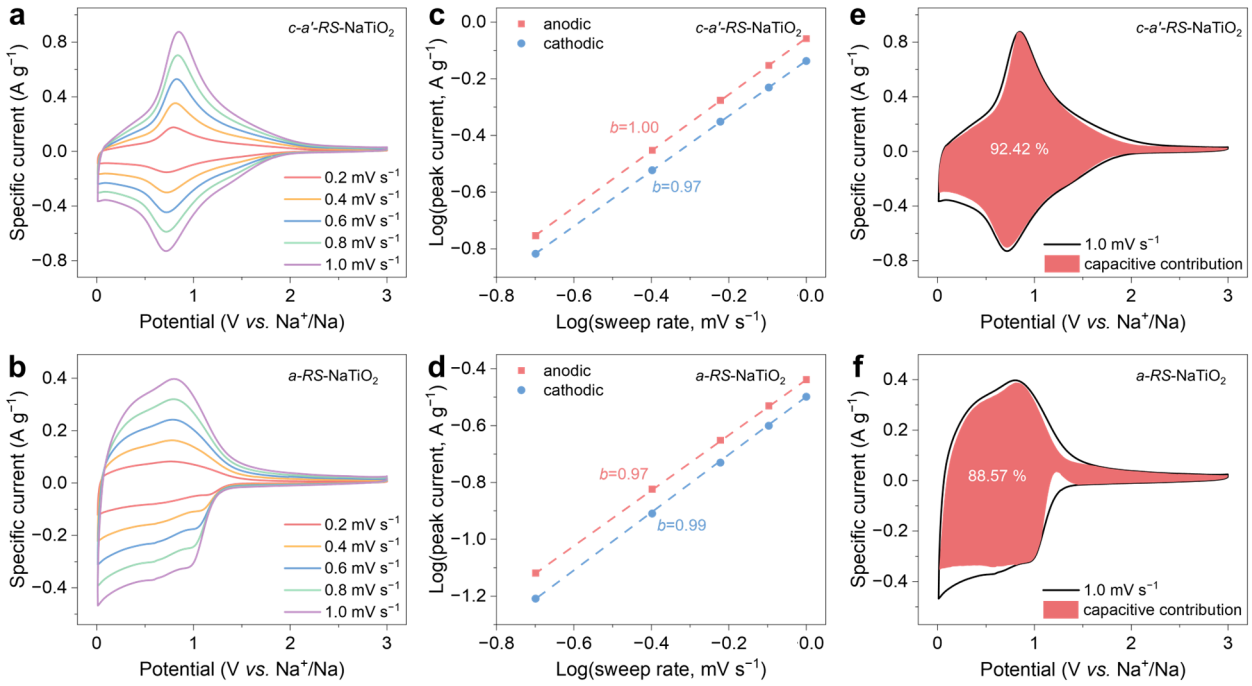

Supplementary Fig. 19. Electrochemical kinetics analysis of the *c-a'-RS*-$NaTiO_2$ and *a-RS*-$NaTiO_2$ electrodes. CV curves of the (**a**) *c-a'-RS*-$NaTiO_2$ and (**b**) *a-RS*-$NaTiO_2$ electrodes at sweep rates of 0.2–1.0 mV s^{-1}. Logarithm peak current *vs.* logarithm sweep rate plots of (**c**) the *c-a'-RS*-$NaTiO_2$ and (**d**) *a-RS*-$NaTiO_2$ electrode. The simulated capacitive contributions of (**e**) the *c-a'-RS*-$NaTiO_2$ and (**f**) *a-RS*-$NaTiO_2$ electrodes at 1.0 mV s^{-1}.

Kinetics analysis was based on the CV measurements (Supplementary Fig. 19a,b). The peak current (i_p) follows the power-law[1] shown in Eq. S1:

$$i_p = av^b \quad \text{(S1)}$$

where the *b*-value of 0.5 represents the semi-infinite diffusion process, and the *b*-value of 1.0 refers to capacitor-like kinetics. The calculated *b*-values of the cathodic and anodic peaks of the *c-a'-RS*-$NaTiO_2$ and *a-RS*-$NaTiO_2$ electrodes are close to 1.0, indicating the domination of capacitive behaviors (Supplementary Fig. 19c,d). The diffusion and capacitive contributions to the total charge storage are separated quantitatively[2] (Eq. S2):

$$i = k_1v + k_2v^{1/2} \quad \text{(S2)}$$

where k_1v is the capacitive contribution and $k_2v^{1/2}$ refers to the diffusion-controlled contribution. The simulated capacitive contributions of the *c-a'-RS*-$NaTiO_2$ and *a-RS*-$NaTiO_2$ electrode are 92.4% and 88.6% , respectively, at 1.0 mV s^{-1} (Supplementary Fig. 19e,f).

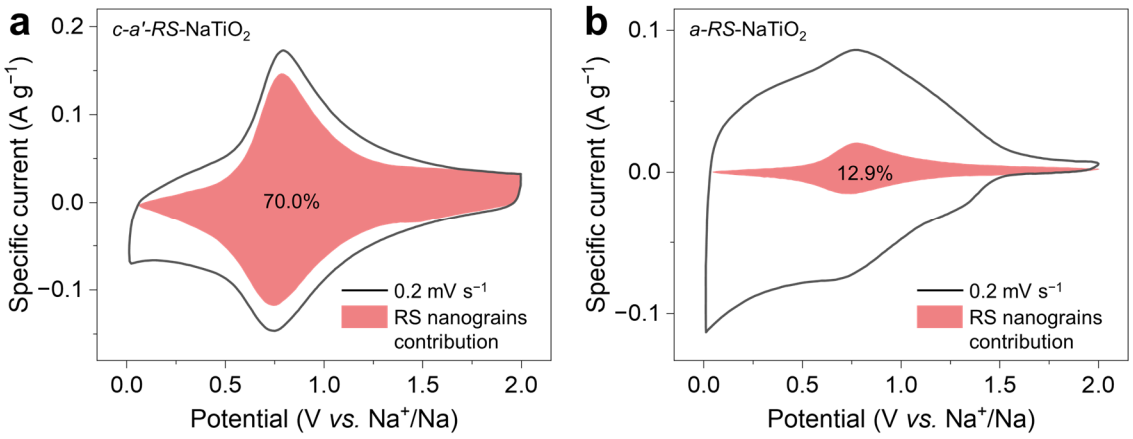

Supplementary Fig. 20. Deconvolution of the response currents. Deconvolution of the response currents from the RS-$NaTiO_2$ and amorphous regions for (**a**) the *c-a'-RS*-$NaTiO_2$and (**b**) *a-RS*-$NaTiO_2$ electrodes.

In our work, the RS nanograins and amorphous regions are coexistent. They both provide the abilities to store Na^+ ions, but exhibit different electrochemical behaviors. The CV curve of the amorphous regions is "box-like" shape, and that of the RS nanograins is "mirror-like" shape. Thus, the total response currents (i_{total}) consist of contributions from the RS phase nanograins (i_{RS}) and the residual amorphous regions (i_{amor}), in which the response currents from electric double-layer capacitance are ignored (Eq. S3):

$$i_{total} = i_{RS} + i_{amor} \tag{S3}$$

The response currents in the 2nd cycle CV curve of *a*-TiO_2 with quasi-rectangular characteristic (i_{rect}) is regarded as the cornerstone of the i_{amor}. At the same time, the response currents with a mirror-like redox couple feature (i_{mirror}) is regarded as the cornerstone of the i_{RS}. Thus, the total response currents are equal to a linear combination of the cornerstone for amorphous regions and the cornerstone for RS nanograins (Eq. S4):

$$i_{total} = i_{RS} + i_{amor} = \mathrm{a}i_{rect} + \mathrm{b}i_{mirror} \tag{S4}$$

Where a and b are positive real constants. The currents contribution in different states of the electrode can be obtained by reasonable simulation. The stored charge is calculated by integrating the response currents over the operating time (Eq. S5).

$$Q = \int_{t_1}^{t_2} i(\mathrm{V})\mathrm{d}t = \frac{1}{v}\int_{t_1}^{t_2} i(\mathrm{V})\mathrm{d}V \tag{S5}$$

Where v is the sweep rate. The operating time is equal to the voltage interval divided by the constant

sweep rate, t=V/v. The total stored charge (Q_{total}) consists of contributions from the RS nanograins (Q_{RS}) and the residual amorphous regions (Q_{amor}), in which the stored charge from electric double-layer capacitance is ignored (Eq. S6):

$$Q_{total} = Q_{RS} + Q_{amor} = \frac{1}{v}\int_{t_1}^{t_2}(i_{RS} + i_{amor})\mathrm{d}V \quad \text{(S6)}$$

By calculating the ratio of the mathematical area of the CV curve for the RS nanograins to the mathematical area of the total CV curve, the capacity contribution of the RS nanograins to the total capacity can be obtained.

The capacity contributions of the RS phase for the *c-a'-RS*-$NaTiO_2$ and *a-RS*-$NaTiO_2$ electrodes are 70.0% (Supplementary Fig. 20a) and 12.9% (Supplementary Fig. 20b), respectively.

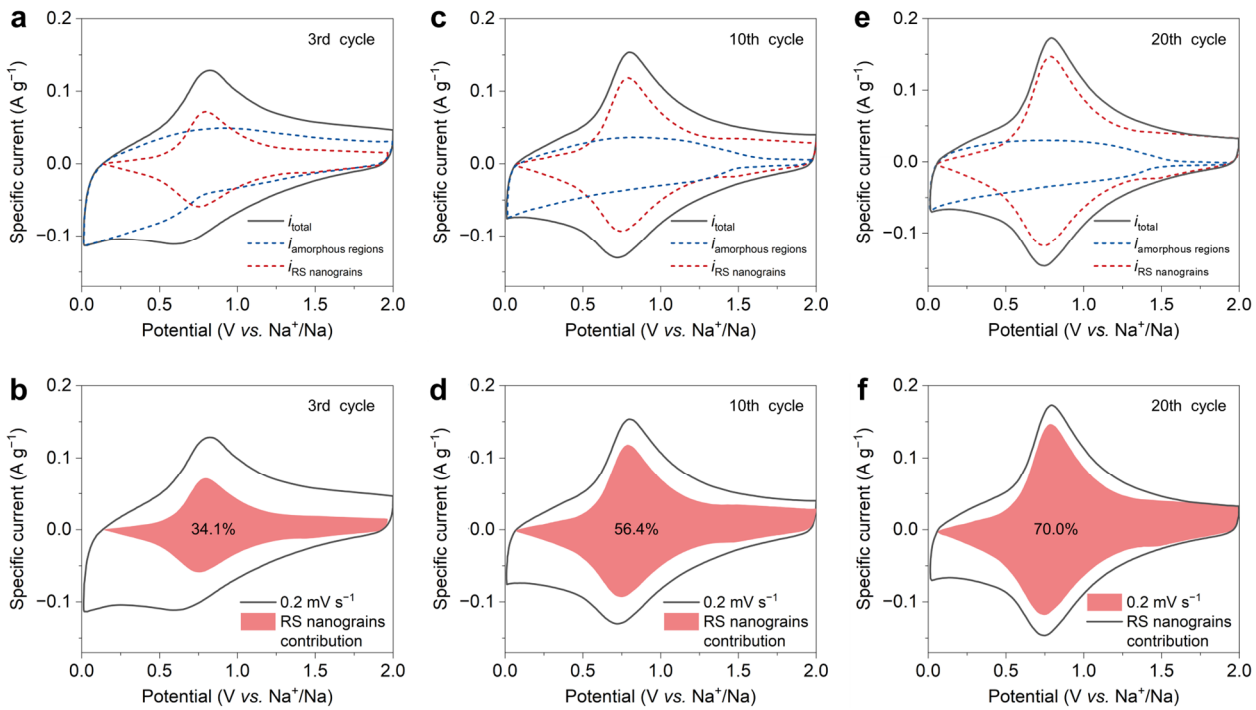

Supplementary Fig. 21. The capacity contribution of the RS nanograins at different cycles. Deconvolution of the CV curves and capacitive contributions to sodium-ion storage at 0.2 mV s^{-1} for the TiO_2(A): (**a**,**b**) at the 3rd cycle, (**c**,**d**) at the 10th cycle, and (**e**,**f**) at the 20th cycle, respectively.

The dynamic changes of the capacity contribution from the RS nanograins and amorphous phase after 3rd, 10th, and 20th cycles were analyzed. The capacity contribution from RS nanograins gradually increases from 34.1% for the 3rd cycle (Supplementary Fig. 21a,b), to 56.4% for the 10th cycle (Supplementary Fig. 21c,d), and to 70% for the 20th cycle (Supplementary Fig. 21e,f), suggesting the growth of RS nanograins during cycling with Na^+. After 20 cycles, the RS nanograins get stable.

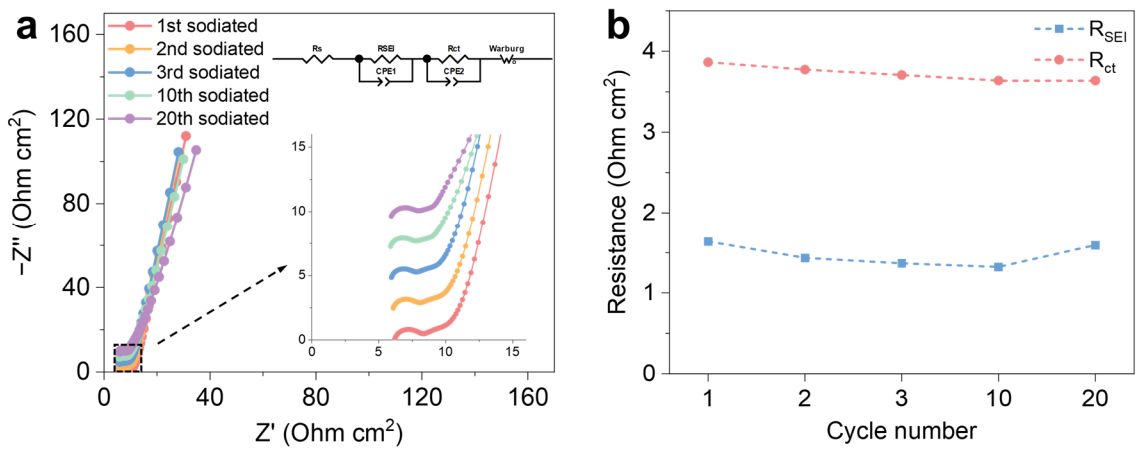

Supplementary Fig. 22. AC impedance tests of the TiO_2(A) electrode after different cycles. (**a**) Nyquist plots of the TiO_2(A) electrode at sodiated state after different cycles. The inset of **a** is the corresponding equivalent circuit. (**b**) The fitted SEI resistance (R_{SEI}) and charge transfer resistance (R_{ct}) after different cycles.

During the 1st sodiation, the electrolyte decomposes and forms the SEI film on the electrode surface, resulting in the generation of R_{SEI}. Then TiO_2(A) undergoes the *c-a'* transformation at low potential, resulting in the increased R_{ct}, which indicates that the appearance of amorphous structure hinders charge transfer processes. During the subsequent *a'-RS* transformation, R_{SEI} slightly changes and R_{ct} decreases with the increase of cycle numbers, indicating that the formation of RS phase reduces the charge transfer resistance.

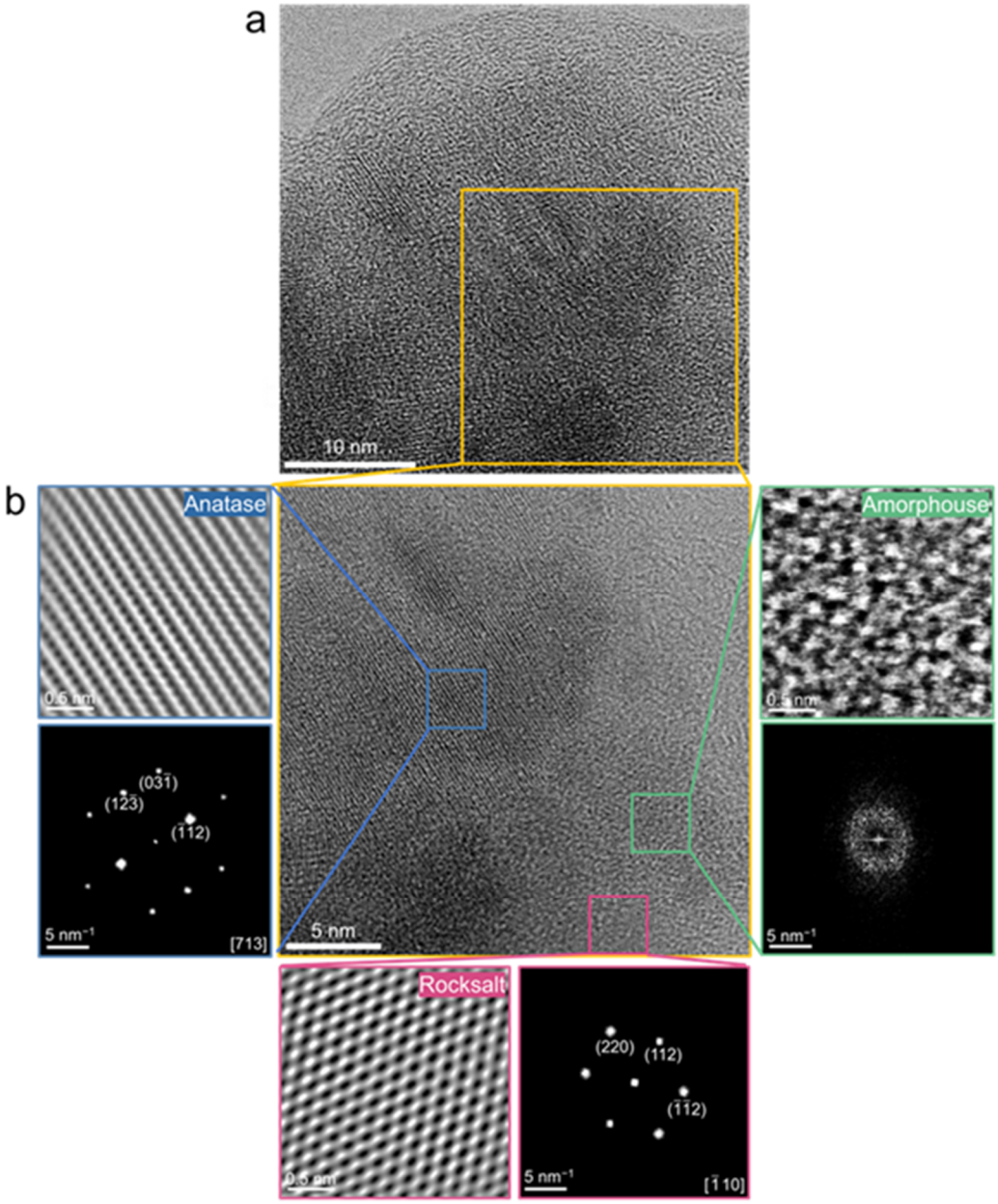

Supplementary Fig. 23. TEM results of the TiO_2(A)-25 nm electrode after 20 cycles. (**a**) HRTEM image of the TiO_2(A)-25 nm electrode after 20 cycles. (**b**) The atomic arrangement diagram and FFT patterns of selected zones, displaying the coexistence of anatase phase, the electrochemically-formed RS phase and some amorphous regions.

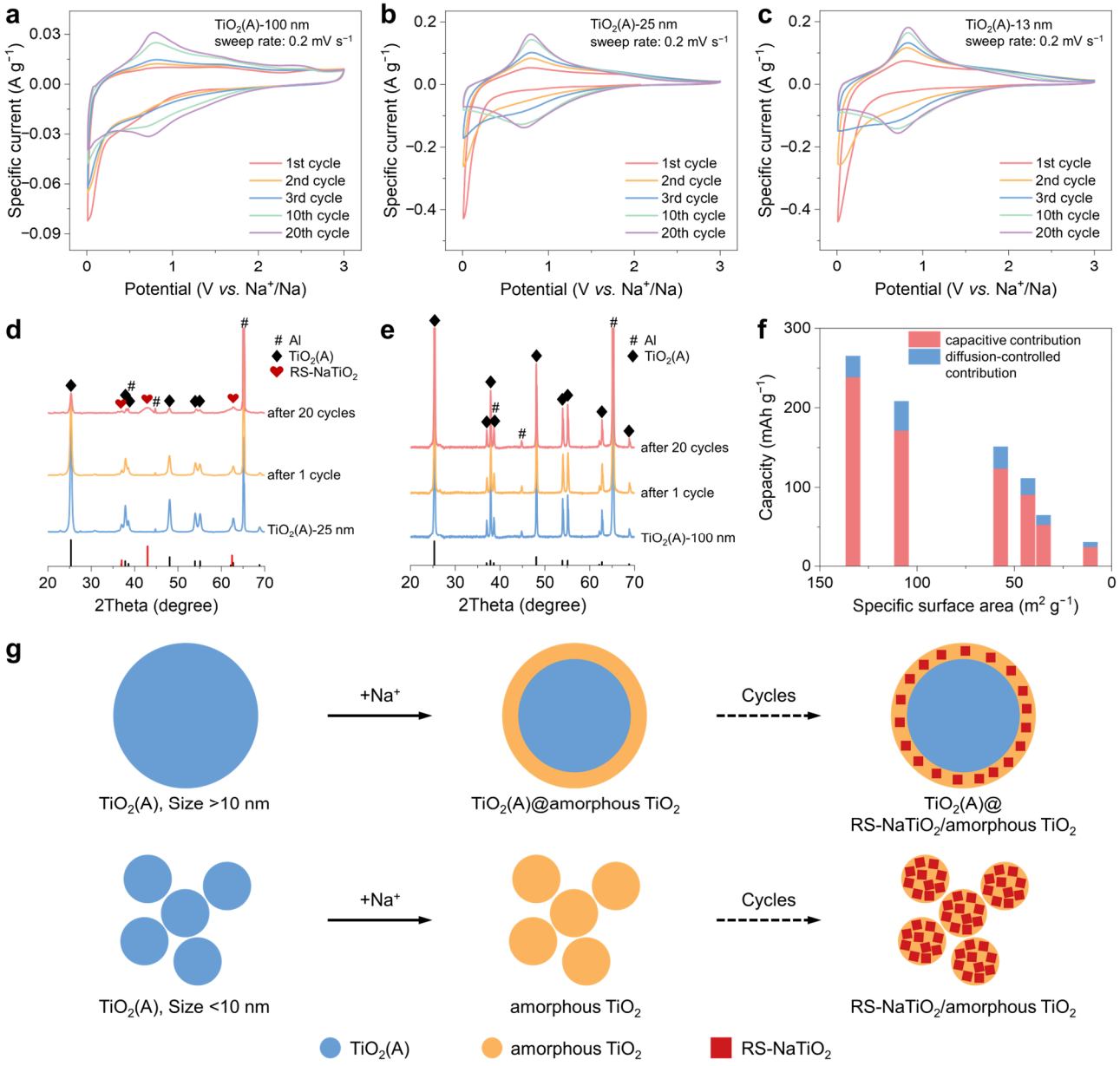

Supplementary Fig. 24. Electrochemical sodium-ion storage properties of TiO_2(A) samples with larger grain sizes. CV curves of the (**a**) TiO_2(A)-100 nm, (**b**) TiO_2(A)-25 nm and (**c**) TiO_2(A)-13 nm samples during the initial 20 cycles at 0.2 mV s^{-1}. Ex situ XRD patterns of (**d**) TiO_2(A)-25 nm and (**e**) TiO_2(A)-100 nm nanoparticles after 20 cycles. (**f**) The polts of specific capacities (at the 20th cycle) *vs.* specific surface areas for the TiO_2(A) samples. (**g**) Schematic of the electrochemical *c-a′-RS* transition of TiO_2(A) samples with different grain sizes.

TiO_2(A) samples with larger grains (Supplementary Fig. 24a–c) show similar changes of CV curves during cycling, indicating multistep *c-a′*-RS transformation. After 20 cycles, they displayed

similar “mirror-like” CV curves with broad redox peaks. During repeated cycles, the limited near-surface regions (~5 nm) turned into the RS-$NaTiO_2$ nanograins, as confirmed by the coexistence of anatase and RS phases in the TiO_2(A)-25 nm sample (Supplementary Fig. 24d). Owing to the limited amount of RS nanograins in the TiO_2(A)-100 nm sample, the diffraction peaks corresponding to the RS phase are not observed (Supplementary Fig. 24e). Importantly, the specific capacities of the TiO_2(A) samples are surface dependent (Supplementary Fig. 24f) owing to the limited thickness of the near-surface active regions[4]. Supplementary Fig. 24g summarizes that the near-surface amorphous regions transform into RS nanograins after long-term cycling with Na^+, ultimately resulting in “mirror-like” CV curves (Fig. 5a and Supplementary Fig. 24a–c).

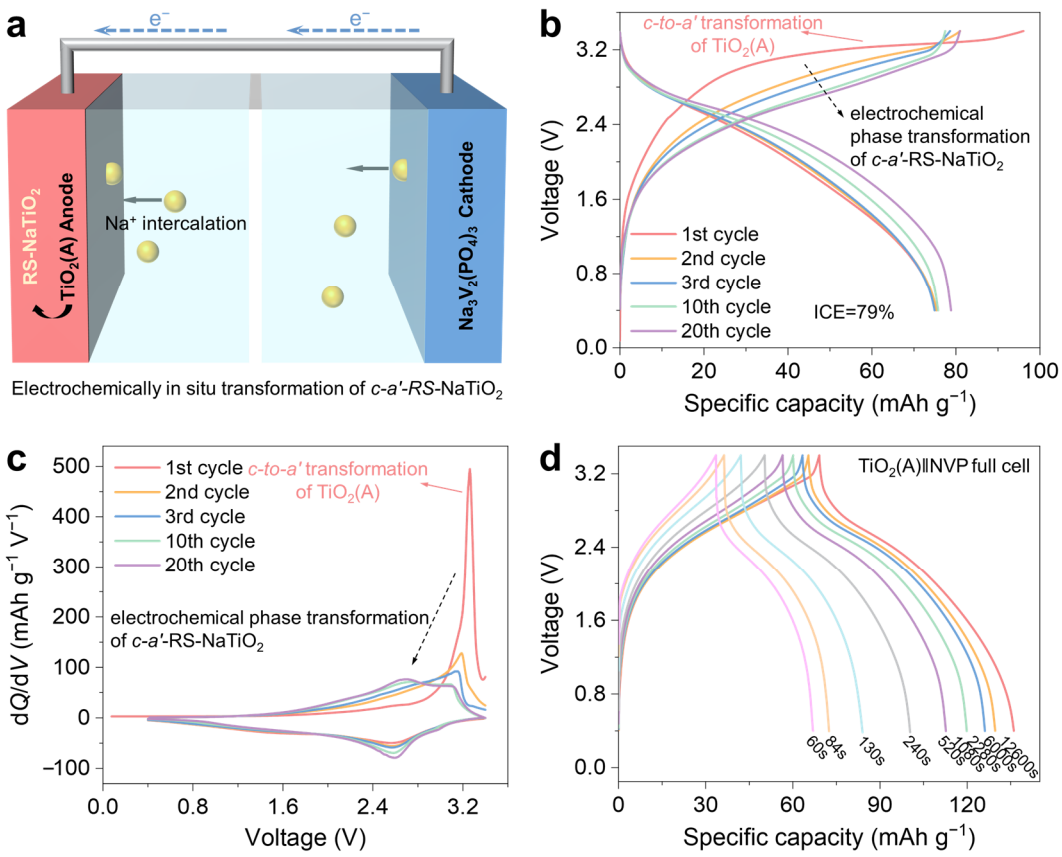

Supplementary Fig. 25. Electrothermally in situ *c-a'-RS* transformation in full cells. (**a**) Schematic of the sodium-ion full cell consisting of the TiO_2(A) anode and $Na_3V_2(PO_4)_3$ cathode. (**b**) GCD profiles and (**c**) related dQ/dV plots of the assembled full cells during the initial 20 cycles in a voltage window of 0.4–3.4 V. (**d**) GCD profiles of the full cells at various specific currents. The capacity was calculated based on the total weight of the $Na_3V_2(PO_4)_3$ and TiO_2(A).

During the initial charge of the full cell (Supplementary Fig. 25a), the plateau at ~3.3 V (Supplementary Fig. 25b) and the sharp peak in the dQ/dV plots (Supplementary Fig. 25c) came from the transformation of anatase to amorphous structure. The continuous changes in the GCD profiles indicated the electrochemical in situ formation of RS-$NaTiO_2$. The above results indicate that the electrothermal in situ activation of TiO_2(A) can be processed in the aging process treatment for the industry of SIBs. The as-assembled SIBs also show fast charging and high-power delivery performances (Supplementary Fig. 25d).

Supplementary Table 1. Summary of the electrochemical properties of representative Ti-based anodes for sodium-ion storage.

Classes	Phase structure	Space group	Morphologies	Reversible capacity (mAh g^{-1})	Potential window (V *vs.* Na^+/Na)	Ref.
Titanium oxides	#Anatase TiO_2 (turned to RS-$NaTiO_2$ after 20 cycles)	*$I4_1/amd$ tuned to $Fm\bar{3}m$*	nanoparticles	253 (after 20 cycles)	0.01−3	This work
	Rutile TiO_2	*$P4_2/mnm$*	nanoparticles	242	0.01−3	5
	Bronze TiO_2	*C2/m*	nanowires	140	0.01−2.5	6
	Amorphous TiO_2	/	architecture	231	0.01−3	7
Titanates	$NaTiO_2$	*$R\bar{3}m$*	microparticles	152	0.6−1.6	8
	$Na_2Ti_2O_5$	*$Pca2_1$*	nanowire arrays	203	0.01−2.5	9
	$Na_2Ti_3O_7$	*$P2_1/m$*	microparticles	195	0.01−3	10
	$Na_2Ti_4O_9$	*C2/m*	micronoodles	125	0.01−2.5	11
	Na_2Ti6O_{13}	*C2/m*	cuboid	188	0.01−2.5	12
	$Li_4Ti_5O_{12}$	*$Fd\bar{3}m$*	nanoparticles	155	0.5−3	13
	$Na_3LiTi_5O_{12}$	*$Fd\bar{3}m$*	microparticles	125	0.3−2	14
Titanium phosphorous	$NaTi_2(PO_4)_3$	*$R\bar{3}c$*	microflowers	125	1.5−3	15
	$NaTiOPO_4$	*$Pna2_1$*	microflakes	88	1−3	16
Ti based-MXenes	Ti_2CT_x	*$P6_3/mmc$*	nanosheets	190	0.1−3	17
	$Ti_3C_2T_x$	*$P6_3/mmc$*	nanosheets	185	0.01−3	18

Note: #According to the findings of this work, the nanosized TiO_2(A) finally turns into RS-$NaTiO_2$ after 20 cycles with Na^+, which determines the electrochemical sodium-ion storage performance.

Supplementary Table 2. Distance of the Ti–O and Ti–Ti pairs in the TiO_2(A) electrode for the initial 20 cycles from ex situ EXAFS spectra.

State	Ti–O (Å)	Ti–Ti (Å)
pristine TiO_2(A)	1.54	2.51
after 1 cycle	1.59	2.76
after 20 cycles	1.55	2.54

Supplementary Table 3. Structural parameters obtained by synchrotron XRD refinement of the RS-$NaTiO_2$ (the 20th sodiated TiO_2(A)).

	Space group	a (Å)	V (Å)	Site occupancy		
				Na(4a)	Ti(4a)	O(4b)
RS-$NaTiO_2$	$Fm\bar{3}m$	4.20464	74.3338	0.5	0.5	1

Supplementary Table 4. Analysis of ex situ Ti 2p XPS peaks for the electrochemically formed *c-a'-RS*-$NaTiO_2$ (the TiO_2(A) electrode after 20 cycles). The peak separation between Ti $2p_{3/2}$ and Ti $2p_{1/2}$ is 5.7 eV and the peak area ratio is 2:1.

Sate	Position (eV)	Ti $2p_{1/2}$ (4+)	Ti $2p_{3/2}$ (4+)	Ti $2p_{1/2}$ (3+)	Ti $2p_{3/2}$ (3+)
		464.2±0.2	458.5±0.2	463.6±0.2	457.9±0.2
20th sodiated	area	538	1076	9122	18244
	percentage	5.6%		94.4%	
	average valence state	3.05			
20th desodiated	area	3152.2	6304.4	1036.8	2073.6
	percentage	75.2%		24.8%	
	average valence state	3.75			

Supplementary Table 5. Distance of the Ti–O and Ti–Ti pairs in the *a*-TiO_2 electrode for the initial 20 cycles from ex situ EXAFS spectra.

State	Ti–O (Å)	Ti–Ti (Å)
pristine *a*-TiO_2	1.60	2.69
after 1 cycle	1.58	2.57
after 20 cycles	1.56	2.55

Supplementary Table 6. The error of R_{SEI} and R_{ct} between the raw and fitted data based on the equivalent circuit.

State	R_{SEI} (Ohm cm^2)	error% (R_{SEI})	R_{ct} (Ohm cm^2)	error% (R_{ct})
1st sodiated	1.64	0.67	3.86	0.89
2nd sodiated	1.43	0.65	3.77	0.83
3rd sodiated	1.37	0.64	3.71	0.87
10th sodiated	1.32	0.82	3.64	1.20
20th sodiated	1.59	0.84	3.62	2.01

Supplementary References

1. Wei, Q. L., et al. Surface-redox sodium-ion storage in anatase titanium oxide. *Nat. Commun.* **14**, 7 (2023).

2. Chang, X. Q., et al. Pseudocapacitive anode materials toward high-power sodium-ion capacitors. *Batteries. Supercaps.* **4**, 1567–1587 (2021).

3. Zheng, L. F., Zhang, L., Zhu, J. G., Wang, G. X.&Jiang, J. C. Co-estimation of state-of-charge, capacity and resistance for lithium-ion batteries based on a high-fidelity electrochemical model. *Applied Energy* **180**, 424–434 (2016).

4. Song, G. R., et al. Physical interpretations of diffusion-controlled intercalation and surface-redox charge storage behaviors. *Energy Storage Mater.* **61**, 102859 (2023).

5. Usui, H., Domi, Y.&Sakaguchi, H. Rutile TiO_2 creates advanced Na-storage materials. *ACS Appl. Energ. Mater.* **6**, 4089–4102 (2023).

6. Liu, S., et al. TiO_2 bunchy hierarchical structure with effective enhancement in sodium storage behaviors. *Carbon Energy* **4**, 645–653 (2022).

7. Zhou, M., et al. Amorphous TiO_2 inverse opal anode for high-rate sodium ion batteries. *Nano Energy* **31**, 514–524 (2017).

8. Wu, D., et al. $NaTiO_2$: a layered anode material for sodium-ion batteries. *Energ. Environ. Sci.* **8**, 195–202 (2015).

9. Que, L. F., Yu, F. D., He, K. W., Wang, Z. B.&Gu, D. M. Robust and conductive $Na_2Ti_2O_5$ nanowire arrays for high performance flexible sodium-ion capacitor. *Chem. Mater.* **29**, 9133–9141 (2017).

10. Pan, H. L., et al. Sodium storage and transport properties in layered $Na_2Ti_3O_7$ for room-temperature sodium-ion batteries. *Adv. Energy Mater.* **3**, 1186–1194 (2013).

11. Kataoka, K.&Akimoto, J. Synthesis and electrochemical sodium and lithium insertion properties of sodium titanium oxide with the tunnel type structure. *J. Power Sources* **305**, 151–155 (2016).

12. Zhang, Y., et al. Sodium titanate cuboid as advanced anode material for sodium ion batteries. *J. Power Sources* **305**, 200–208 (2016).

13. Sun, Y., et al. Direct atomic-scale confirmation of three-phase storage mechanism in $Li_4Ti_5O_{12}$ anodes for room-temperature sodium-ion batteries. *Nat. Commun.* **4**, 1870 (2013).

14. Kitta, M., Kojima, T., Kataoka, R., Yazawa, K.&Tada, K. Realizing the single-phase spinel-type sodium titanium oxide with the $Li_4Ti_5O_{12}$-like structure for building stable sodium-ion batteries. *ACS Appl. Mater. Inter.* **12**, 9322–9331 (2020).

15. Xu, C., et al. Carbon-coated hierarchical $NaTi_2(PO_4)_3$ mesoporous microflowers with superior sodium storage performance. *Nano Energy* **28**, 224–231 (2016).

16. Mu, L. Q., et al. Novel 1.5 V anode materials, $ATiOPO_4$ (A=NH_4, K, Na), for room-temperature sodium-ion batteries. *J. Mater. Chem. A* **4**, 7141–7147 (2016).

17. Wang, X., et al. Pseudocapacitance of MXene nanosheets for high-power sodium-ion hybrid capacitors. *Nat. Commun.* **6**, 6544 (2015).

18. Liu, S. Y., et al. A novel strategy of in situ trimerization of cyano groups between the $Ti_3C_2T_x$ (MXene) interlayers for high-energy and high-power sodium-ion capacitors. *Nano-Micro Lett.* **12**, 135 (2020).